04 May 2010

Structural Damage Detection Robust Against Time Synchronization Errors

Guirong Yan
Missouri University of Science and Technology, yang@mst.edu

Shirley J. Dyke

Recommended Citation

Structural damage detection robust against time synchronization errors

To cite this article: Guirong Yan and Shirley J Dyke 2010 *Smart Mater. Struct.* **19** 065001

View the article online for updates and enhancements.

Structural damage detection robust against time synchronization errors

Guirong Yan[1,2,3,4] and Shirley J Dyke[2]

[1] School of Engineering, University of Western Sydney, Penrith, NSW 1797, Australia
[2] School of Mechanical Engineering, Purdue University, West Lafayette, IN 47907, USA
[3] School of Civil Engineering, Harbin Institute of Technology, Harbin, 150090,
People's Republic of China

E-mail: g.yan@uws.edu.au and sdyke@purdue.edu

Abstract
Structural damage detection based on wireless sensor networks can be affected significantly by time synchronization errors among sensors. Precise time synchronization of sensor nodes has been viewed as crucial for addressing this issue. However, precise time synchronization over a long period of time is often impractical in large wireless sensor networks due to two inherent challenges. First, time synchronization needs to be performed periodically, requiring frequent wireless communication among sensors at significant energy cost. Second, significant time synchronization errors may result from node failures which are likely to occur during long-term deployment over civil infrastructures. In this paper, a damage detection approach is proposed that is robust against time synchronization errors in wireless sensor networks. The paper first examines the ways in which time synchronization errors distort identified mode shapes, and then proposes a strategy for reducing distortion in the identified mode shapes. Modified values for these identified mode shapes are then used in conjunction with flexibility-based damage detection methods to localize damage. This alternative approach relaxes the need for frequent sensor synchronization and can tolerate significant time synchronization errors caused by node failures. The proposed approach is successfully demonstrated through numerical simulations and experimental tests in a lab.

(Some figures in this article are in colour only in the electronic version)

1. Introduction

Recent catastrophic failures of civil engineering structures around the world (for example, I-35W highway bridge over the Mississippi River in Minneapolis, Minnesota, US, 2007) underscore the need for reliable and robust structural health monitoring (SHM) systems. To make timely decisions regarding reinforcement and maintenance strategies, these SHM systems should be capable of collecting structural response data, identifying the existence or onset of damage in structures, localizing and quantifying the damage, and tracking down processing of damage as well as estimating the remaining life and capacity of the structure. To this end, effective damage detection algorithms must be integrated into these SHM systems.

Although, to date, a large number of damage detection methods have been proposed and the effectiveness of these methods has been demonstrated through numerical simulations or laboratory experiments, conventional SHM systems integrated with these methods often fail to fully achieve their anticipated functionality in real-world applications. One reason for such failure is that relatively few measurement points are typically deployed in a structure because the sensor system in a traditional SHM system is cable based, and it is very expensive and labor intensive to install a large number of sensors. With recent technological advances in wireless communication, SHM systems based on a wireless sensor network (WSN) may provide a feasible solution [1–3]. WSNs have several advantages over most traditional SHM systems, such as low installation and maintenance costs, relatively less installation time, reprogrammable ability and convenient reconfiguration capacity. Thus, a dense deployment of

---

[4] Author to whom any correspondence should be addressed.

Table 1. Actual clock readings of the reference sensor node and the ith sensor node.

	After the first 2 h	After an integer (M) multiple of 2 h periods
At the reference sensor node	$t = 2\,\text{h} \times 60\,\text{min h}^{-1} \times 60\,\text{s min}^{-1}$	$t = M \times 2\,\text{h} \times 60\,\text{min h}^{-1} \times 60\,\text{s min}^{-1}$
At the ith sensor node	$t_i = t + \alpha_i t + \delta t_i$	$t_i = t + \alpha_i t + \delta t_i$
TSE at the beginning of next block of data sensing	$\text{TSE} = t_i - t = \alpha_i \times 2 \times 60 \times 60\,\text{s} + \delta t_i$	$\text{TSE} = t_i - t = \alpha_i \times M \times 2 \times 60 \times 60\,\text{s} + \delta t_i$

measurement points in a SHM system becomes quite feasible with WSNs. Researchers have successfully implemented these networks with a variety of damage detection strategies on several systems [4–9].

However, unlike conventional SHM where cable-based systems are properly configured, SHM with WSN systems faces new challenges related to the inability of the sensors to sample data simultaneously, resulting in significant time synchronization errors (TSEs) between different wireless sensing units. These TSEs may be attributed to both clock drift and clock offset between wireless sensors [10]. Clock drift exists because the actual oscillation frequency of a clock crystal is not precisely its design frequency, and also because the frequency may change over time due to environmental factors such as variations in temperature, supply voltage and shock as well as oscillator aging. Clock offsets exist because it is infeasible to initialize all the nodes in a WSN at the exact same moment, and hence each sensor's clock has its own initial time.

Several time synchronization protocols have been proposed for WSNs that aim to reduce TSEs by allowing nodes to agree on a single reference time. These methods can be classified into the following three groups: receiver–receiver synchronization-based algorithms (such as the reference broadcast synchronization (RBS) [10]), pair-wise synchronization-based algorithms (such as the timing-sync protocol for sensor networks (TPSN) [11]) and sender–receiver synchronization-based algorithms (such as the flood time synchronization protocol (FTSP) [12] and delay measurement time synchronization (DMTS) [13]). These methods provide different mechanisms to synchronize local clocks of sensor nodes within a WSN.

Even when these protocols are employed, completely synchronized measurements are not guaranteed. Assuming that a single sensor in the network is designated as the reference sensor, all other nodes in the network will attempt to synchronize against the reference's clock. The relationship between the clock reading of the ith wireless sensor and that of the reference clock is as follows

$$t_i = (1 + \alpha_i)t - \delta t_i = t + \alpha_i t - \delta t_i \qquad (1)$$

where t_i and t denote the clock readings of the ith wireless sensor and the reference sensor, respectively. α_i and δt_i are the clock drift rate and initial clock offset of the ith wireless sensor compared with the reference sensor. The $\alpha_i t$ factor corresponding to the clock drift will cause TSE to accumulate over time, even when a time synchronization protocol is able to compensate for the initial clock offset (δt_i).

To demonstrate the accumulation of TSE, table 1 lists sample clock readings and TSEs in a WSN which starts to collect data every two hours and stops collecting data after acquiring N data points. The total TSE is the sum of the initial clock offset δt_i and the TSE resulting from clock drift. δt_i can be assumed to be very small if time synchronization is performed when the system initializes. The TSE caused by clock drift continuously increases with time (for instance, on typical WSN sensor platforms, this effect can be as large as 40–50 μs s^{-1} [14, 22]). It is worth noting that the total TSE at the end of one 2 h operation may be viewed as the initial clock offset for the next block of sensing. Therefore, the longer the operating time of the WSN, the larger the clock offset for a given block caused by clock drift, and accordingly, the larger the total TSE.

One strategy to combat the increasing TSE is to periodically re-synchronize the entire network against the reference clock. It is well known that FTSP uses the effect of clock drift between periodic re-synchronizations to estimate each node's clock drift rate α_i. Nevertheless, TSE cannot be completely eliminated under FTSP due to errors in estimating the clock drift, particularly in an operating SHM system where these errors can be amplified by node failures. An implementation of FTSP on a testbed of Berkeley Mica2 sensors accumulated over 60 μs of TSE in the face of node failure, even under an unrealistically aggressive schedule that re-synchronized the entire network every 30 s. Furthermore, time synchronization in a WSN requires that wireless sensors exchange information, which consumes energy. In addition, when sensing is in progress, time synchronization may not perform well [14].

Clearly, full realization of synchronized sensing is quite challenging. Prior research suggests that the presence of TSEs has impacts on system identification and damage detection results. Nagayama [14] investigated the effect of TSEs both on the transfer function between an input force and sensor response and on the correlation function of responses, and found that the identified natural frequencies and damping ratios were not affected, while phase errors did occur in the identified mode shapes. Krishnamurthy *et al* [15] also observed that TSEs affect the amplitudes of identified mode shapes.

In this study, the goal of performing accurate damage detection in a WSN having TSEs will be addressed from a new perspective. Our goal is not to implement a new time synchronization approach, but rather to enhance the robustness of damage detection approaches against TSEs and avoid the need for frequent time synchronization in a WSN, resulting in diminished energy consumption. First, we will systematically investigate the influence of TSEs on the magnitude and phase

of identified mode shapes and examine how one might exploit this knowledge for accurate damage detection. Then, two damage detection methods that are tolerant to TSEs are proposed. The efficacy of these approaches is demonstrated through numerical simulations on a simply supported beam and a planar truss. In addition, these approaches are validated through experimental tests in a laboratory.

2. Background

2.1. System identification using the FDD method

When monitoring in-service civil engineering structures, the primary sources of external excitations are ambient vibrations such as those caused by wind or traffic loads. Because ambient excitation sources are often unmeasurable, only the resulting structural responses, the system outputs, can be reliably used for system identification and damage detection. One effective method for output-only modal identification is the frequency domain decomposition (FDD) method [16].

In the FDD method, the cross spectral density (CSD) matrix of the response is first estimated, expressed as (assuming that the pth discrete frequency is associated with the mth natural frequency)

$$\mathbf{G}(\omega_m) = \mathbf{G}(p)$$
$$= \begin{bmatrix} X_1(p)X_1^*(p) & \cdots & X_1(p)X_i^*(p) & \cdots & X_1(p)X_n^*(p) \\ \vdots & & \vdots & & \vdots \\ X_i(p)X_1^*(p) & \cdots & X_i(p)X_i^*(p) & \cdots & X_i(p)X_n^*(p) \\ \vdots & & \vdots & & \vdots \\ X_n(p)X_1^*(p) & \cdots & X_n(p)X_i^*(p) & \cdots & X_n(p)X_n^*(p) \end{bmatrix}$$
$$(2)$$

where $X_i(p)$ represents the discrete Fourier transform (DFT) of the response at the ith DOF, and $\cdot^*$ represents the conjugate transpose operation. To minimize the impact of measurement noise, the averaged CSD matrix is obtained by performing an averaging operation on the CSD matrices estimated from multiple frames of data.

A singular value decomposition (SVD) is performed then on the averaged CSD matrix at each discrete frequency. The maximum singular value in each singular value matrix is collected to form a vector. From the peaks of this vector, the natural frequencies are identified. The first column of the left singular decomposition matrix corresponding to a particular natural frequency is an estimate of the corresponding mode shape. In the implementation discussed herein, because only output information is used for identification, the identified results from the FDD method are actually operational deflection shapes (OPS).

Assume $\mathbf{U}_1$ is the estimate of the mth mode shape. By dividing all of the components of $\mathbf{U}_1$ by the component of $\mathbf{U}_1$ chosen as the reference, the normalized mode shape is obtained with one component having a value of one. Its components are, in general, complex values. The phase associated with each complex value represents the phase difference between that response location and the reference sensor location in the mth mode. To obtain real-valued

components of a mode shape, which are typically used for damage detection methods, the magnitude of each component of the normalized $\mathbf{U}_1$ is calculated. The corresponding sign for each component is determined by its respective phase. The phases of the components in the normalized mode shape are ideally equal to 0 or π for proportionally damped systems with no measurement error. If the phase is 0, the corresponding sign is taken as positive; if the phase is π, the corresponding sign is taken as negative. In practice, due to measurement and numerical errors, the phases are not exactly 0 or π. Therefore, the signs of the components are determined in the following way here: if the phase is in the range of $[-\frac{\pi}{2} \quad \frac{\pi}{2}]$, the corresponding sign will be positive; otherwise, if the phase is in the range of $[\frac{\pi}{2} \quad \frac{3\pi}{2}]$, the corresponding sign will be negative.

2.2. Damage detection using flexibility-based methods

Techniques for damage detection based on structural flexibility have been gaining attention [17–19]. A good estimate of the flexibility matrix can be obtained with easily identified low-frequency modes, making flexibility-based methods attractive for civil engineering applications. Also, the flexibility matrix corresponding to the sensor coordinates can be extracted directly from the matrices of system realization. For these reasons, and due to their success in the prior studies mentioned previously, flexibility-based methods are employed in this study.

2.2.1. Classical flexibility difference method. Based on the assumption that the presence of damage in structures reduces structural stiffness and thus increases structural flexibility, the change in structural flexibility between the pre- and post-damaged states can be used to detect damage. The change in classical flexibility matrix $\mathbf{F}$ can be computed as

$$\Delta \mathbf{F} = |\mathbf{F}^{\mathrm{d}} - \mathbf{F}^{\mathrm{u}}| \qquad (3)$$

where $|\cdot|$ denotes the absolute value of a matrix; the superscripts d and u indicate the damaged and undamaged structures, respectively. Each of the flexibility matrices can be assembled from the modal parameters using

$$\mathbf{F} = \sum_{r=1}^{n} \frac{1}{\omega_r^2} \boldsymbol{\varphi}_r \boldsymbol{\varphi}_r^T \qquad (4)$$

where ω_r and $\boldsymbol{\varphi}_r$ are the rth mass-normalized mode shape and circular modal frequency, respectively, and n is the number of modes used. In the classical flexibility difference method, the diagonal entries or the maximum absolute values of the elements in each column of $\Delta \mathbf{F}$ are extracted to form a vector, yielding damage locations [20].

2.2.2. ASH flexibility-based method. Because the damage detection results using classical flexibilities are embodied as a nodal or degree of freedom (DOF) characterization, the classical flexibility difference method cannot directly localize damage to exact elements. Consequently, the ASH flexibility-based method [21] was proposed for localizing damage in beam-like structures. This method determines the change in

angles-between-string-and-horizon (ASHs) of beam elements caused by damage, and thus it can localize damage to exact elements. The ASH flexibility matrix can be constructed as

$$\mathbf{F}_\theta = \sum_{r=1}^{n} \frac{1}{\omega_r^2} \mathbf{R}_r \mathbf{R}_r^T \tag{5}$$

where $\mathbf{R}_r$ is called the th ASH mode shape, which can be expressed in terms of the rth translational mode shape as

$$\mathbf{R}_r = [\; \tfrac{1}{l_1}\varphi_{1,r} \quad \tfrac{1}{l_2}(\varphi_{2,r} - \varphi_{1,r}) \quad \cdots \quad \tfrac{1}{l_i}(\varphi_{i,r} - \varphi_{i-1,r})$$
$$\cdots \quad \tfrac{1}{l_n}(\varphi_{n,r} - \varphi_{n-1,r}) \;]^T \tag{6}$$

where $\varphi_{i,r}$ denotes the ith component of the rth mode shape, and l_i denotes the length of the ith beam element. The components in the rth column of this flexibility matrix represent the ASHs of all beam elements of the structure resulting from a unit moment applied at two nodes of element r, with no force or moment on the other elements. Thus, the components in the ASH flexibility are associated with beam elements rather than nodes.

The diagonals or the maximum absolute values of the components in each column in the difference of ASH flexibility matrices between the pre- and post-damaged structures are extracted as damage indicators. By observing a 'step and jump' in the plot of damage indicators versus element numbers, the damage locations are determined.

3. Influence of TSEs on mode shape identification

In this section, the effect of TSEs on the identified results of mode shapes is first investigated. Then a strategy for modifying the distorted mode shapes to be suitable for damage detection is proposed.

Consider first the impact of various TSE sources. When TSEs exist among a set of wireless sensors, the sensors start to acquire data at different times and two sensors may even acquire the data at different sampling frequencies. Assume we have two sensors measuring response data at the same DOF, denoted the ith DOF. Assume that one sensor's clock is taken as the reference clock and its time t is used as the time base. This sensor acquires data using the reference clock, and the other sensor acquires data using its own local clock. Here, the two sets of data collected by the reference sensor and the other sensor at the same location (say, at DOF i) are designated $x_i(t)$ and $\tilde{x}_i(t)$, respectively. The two sets of data are related by

$$\tilde{x}_i(t) = x_i((1 + \alpha_i)t - \delta t_i) \tag{7}$$

where α_i is the clock drift rate and δt_i is the initial clock offset of the other sensor relative to the reference sensor.

Prior research suggests that the clock drift rate α_i is usually relatively small, e.g., Shamm *et al* [22] observed that the frequency differences of the crystals used in Mica2 motes introduced a drift of 40 μs s^{-1}. Nagayama *et al* [14] estimated the maximum α_i among one set of Imote2 nodes to be approximately 50 μs s^{-1}. Therefore, for a frame of measured data with relatively short length, the effect of α_i on this frame of data is negligible, and all the accumulated TSE

caused by α_i before can be included in δt_i, as discussed in section 1. Thus equation (7) can be written as

$$\tilde{x}_i(t) = x_i(t + \delta t_i). \tag{8}$$

Performing a Fourier transform (FT) of both sides of equation (8) yields

$$\tilde{X}_i(\omega) = \mathbb{F}[\tilde{x}_i(t)] = \mathbb{F}[x_i(t + \delta t_i)] = e^{i\omega \delta t_i} X_i(\omega) \tag{9}$$

where $\mathbb{F}[\cdot]$ represents the FT operation. $\tilde{X}_i(\omega)$ and $X_i(\omega)$ are the FTs of $\tilde{x}_i(t)$ and $x_i(t)$, respectively. Equation (9) suggests that δt_i introduces a phase shift of $\omega_m \delta t_i$ to the frequency domain representation of the response. However, equation (9) only applies to the continuous Fourier transform of data under ideal conditions. In practice, the discrete Fourier transform (DFT) is used, and thus we really need to explore the relationship between the DFTs of the data with and without TSEs. Consider one set of digital data $x(n)$ as the data without a TSE (reference) and another set of data $\tilde{x}(n)$ as the data with a TSE (for illustration, we consider a time shift of two time steps here). Thus, the data obtained are

$$\begin{aligned} x(n) &= [\; x(1) \quad x(2) \quad \cdots \quad x(N-1) \quad x(N) \;] \\ \tilde{x}(n) &= [\; x(3) \quad x(4) \quad \cdots \quad x(N+1) \quad x(N+2) \;] \end{aligned} \tag{10}$$

and the DFTs of $x(n)$ and $\tilde{x}(n)$ can be expressed as

$$X(k) = \sum_{n=1}^{N} x(n) e^{-j\frac{2\pi(n-1)k}{N}} \tag{11}$$

$$\tilde{X}(k) = \sum_{n=1}^{N} \tilde{x}(n) e^{-j\frac{2\pi(n-1)k}{N}} \tag{12}$$

where k is the frequency domain variable. If the two sides of equation (12) are multiplied by $e^{-j\frac{2\pi \cdot 2 \cdot k}{N}}$ and then subtracted from equation (11), rearranging this equation yields the relationship between $\tilde{X}_i(k)$ and $X_i(k)$:

$$\tilde{X}(k) = (X(k) + (x(N+1) - x(1)) e^{-j\frac{2\pi \cdot 0 \cdot k}{N}} + (x(N+2) - x(2)) e^{-j\frac{2\pi \cdot 1 \cdot k}{N}}) e^{j\frac{2\pi \cdot 2 \cdot k}{N}}. \tag{13}$$

Clearly, all terms except the $X(k)$ term on the right-hand side of equation (13) are caused by the TSE. A larger TSE will result in more terms in the parentheses on the right-hand side of equation (13). To better understand the influence of the TSE on the magnitude of $\tilde{X}(k)$, the magnitudes of both sides of equation (13) are obtained, yielding

$$|\tilde{X}(k)| = |X(k) + (x(N+1) - x(1)) e^{-j\frac{2\pi \cdot 0 \cdot k}{N}} + (x(N+2) - x(2)) e^{-j\frac{2\pi \cdot 1 \cdot k}{N}}|. \tag{14}$$

Note that the term outside of the parentheses on the right side of equation (13) has a magnitude of one. From equation (14) it is clear that $|\tilde{X}(k)| \neq |X(k)|$. That is, the TSE introduces an error in the magnitude of the DFT of $\tilde{x}(n)$ as compared to that of $x(n)$. However, if the TSE is not very significant, this error will be small enough to be negligible for the purpose of application of the FDD method. This conclusion can be explained by considering equation (14) and noting that
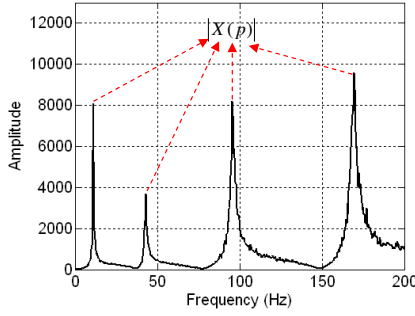
Figure 1. Amplitude of the DFT of response.

in the FDD method we just use the values of the DFTs at each mode of the structure (i.e., DFTs associated with natural frequencies). In the sequel, we just examine the discrete frequency associated with a particular mode, and the frequency variable is designated p which is assumed to correspond to the mth mode. Thus, if this mode is excited properly, $|X(p)|$ will exhibit a peak in the amplitude spectrum of the DFT, as illustrated in figure 1. $|X(p)|$ and its real and/or imaginary parts are, in practice, large in magnitude compared to the other terms in the parentheses. Therefore, the difference between $|\tilde{X}(p)|$ and $|X(p)|$ is small enough to be negligible.

Regarding the influence of the TSE on the phase of the DFT of $\tilde{x}(n)$, two sources of phase distortion must be examined. One is due to the two terms in the parentheses on the right-hand side of equation (13). Herein we call the phase distortion contributed by these terms 'phase error'. The second is due to the term $e^{j\frac{2\pi \cdot 2 \cdot p}{N}}$ outside of the parentheses. Here we call $\frac{2\pi \cdot 2 \cdot p}{N}$ the 'phase shift'. For the first source, consider the part in the parentheses as the sum of three vectors in a complex plane. As was discussed before, the vector $X(p)$ is very large in magnitude, and the other two terms are relatively small. Therefore, the phase error caused by these two terms will be small when the delay is not very significant. However, the impact of the phase shift is significant and cannot be ignored.

Based on the above discussion, for a particular mode of the structure, equation (13) can be approximated as

$$\tilde{X}(p) \approx X(p)e^{j\frac{2\pi \cdot 2 \cdot p}{N}}. \tag{15}$$

In general, if the time shift between the two signals is Δn, the phase error between the two DFTs will be $\frac{2\pi \cdot \Delta n \cdot p}{N}$, which can be rearranged as

$$\frac{2\pi \cdot \Delta n \cdot p}{N} = \frac{2\pi \cdot \Delta n \cdot p}{N} \cdot \frac{\Delta f}{\Delta f} = 2\pi f_m \frac{\Delta n}{f_s} = \omega_m \delta t. \tag{16}$$

Note that the pth frequency point is associated with the mth natural frequency of the structure, ω_m. Δf is the frequency resolution of the DFT, and $\frac{\Delta n}{f_s}$ is the TSE δt which could be a non-integer time step shift.

Based on equations (15) and (16), the DFT of the response $\tilde{x}_i(t)$ at the mth mode can be expressed as

$$\tilde{X}_i(p) \approx X_i(p)e^{j\omega_m \delta t_i}. \tag{17}$$

Equation (17) suggests that, in practice, the TSE not only introduces a phase shift of $\omega_m \delta t_i$ in the frequency domain, but

also introduces an error in the amplitude and an error in the phase (other than the phase shift of $\omega_m \delta t_i$), which is reflected by the symbol of '$\approx$' in equation (17). However, these two errors are small enough to be negligible when the TSE is not very significant. Thus, we conclude that the main impact of the TSE on the frequency domain representation lies in the phase shift caused by the term of $e^{j\omega_m \delta t_i}$ in equation (17).

Using equation (17) we will consider the impact of the TSEs on the identified mode shapes. To facilitate the analysis, let us rearrange the CSD matrix at the mth natural frequency in equation (2) as

$$\mathbf{G}(\omega_m) = \mathbf{G}(p)$$
$$= \begin{bmatrix} X_1(p) \\ \vdots \\ X_i(p) \\ \vdots \\ X_n(p) \end{bmatrix} [\, X_1^*(p) \quad \cdots \quad X_i^*(p) \quad \cdots \quad X_n^*(p) \,]. \tag{18}$$

In addition, we can replace the SVD in the traditional FDD method with an eigenvalue decomposition because the mode shapes are only related to the left singular decomposition matrices. The SVD of a CSD matrix at $\omega = \omega_m$ can be calculated by means of solving an eigenvalue problem [23] as follows

$$\mathbf{G}(\omega_m)\mathbf{G}^*(\omega_m) = \mathbf{U}\Sigma^2\mathbf{U}^* = \mathbf{U}\Sigma\Sigma^*\mathbf{U}^*. \tag{19}$$

Therefore, let

$$\mathbf{G}(\omega_m) = \mathbf{U}\Sigma \tag{20}$$

where Σ and $\mathbf{U}$ denote the singular value matrix and the left singular decomposition matrix, respectively. Σ is a diagonal matrix. Herein the first column of $\mathbf{U}$, an estimate of the mth mode shape, is designated $\mathbf{U}_1$. As in equation (18), the CSD matrix of the responses with TSEs is written as

$$\tilde{\mathbf{G}}(\omega_m) = \tilde{\mathbf{G}}(p) = \begin{bmatrix} \tilde{X}_1(p) \\ \vdots \\ \tilde{X}_i(p) \\ \vdots \\ \tilde{X}_n(p) \end{bmatrix}$$
$$\times [\, \tilde{X}_1^*(p) \quad \cdots \quad \tilde{X}_i^*(p) \quad \cdots \quad \tilde{X}_n^*(p) \,]. \tag{21}$$

Extending equation (17) to multiple sensors, each having a different TSE, and substituting the results into equation (21) yields

$$\tilde{\mathbf{G}}(\omega_m) \approx \mathbf{P}\mathbf{G}(\omega_m)\mathbf{P}^* \tag{22}$$

where $\mathbf{P}$, in the sequel, is called the time synchronization error matrix, and is expressed as

$$\mathbf{P} = [\, e^{i\omega_m \delta t_1} \quad \cdots \quad e^{i\omega_m \delta t_i} \quad \cdots \quad e^{i\omega_m \delta t_n} \,]. \tag{23}$$

To identify the mode shapes, an eigenvalue decomposition is performed on $\tilde{\mathbf{G}}(\omega_m)\tilde{\mathbf{G}}^*(\omega_m)$ as in equation (19). From equations (22) and (20), $\tilde{\mathbf{G}}(\omega_m)\tilde{\mathbf{G}}^*(\omega_m)$ can be expressed as

$$\tilde{\mathbf{G}}(\omega_m)\tilde{\mathbf{G}}^*(\omega_m) \approx \mathbf{P}\mathbf{G}(\omega_m)\mathbf{P}^*(\mathbf{P}^*)^*\mathbf{G}^*(\omega_m)\mathbf{P}^*$$
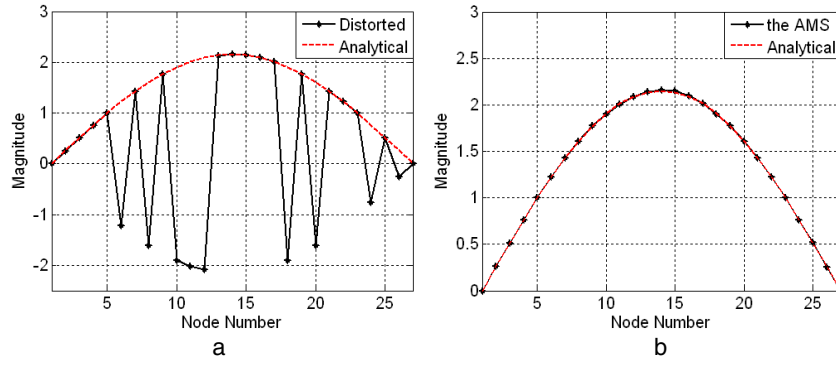$$= \mathbf{P}\mathbf{U}\Sigma\mathbf{P}^*\mathbf{P}\Sigma^*\mathbf{U}^*\mathbf{P}^*. \tag{24}$$

Figure 2. Adjusted first mode shape of a simply supported beam. (a) 1st identified mode shape and (b) 1st AMS after sign adjustment.

Because Σ and $\mathbf{P}$ are diagonal matrices, equation (24) can be rearranged as

$$\tilde{\mathbf{G}}(\omega_m)\tilde{\mathbf{G}}^*(\omega_m) \approx \mathbf{P}\mathbf{U}\mathbf{P}^*\Sigma\Sigma^*\mathbf{P}\mathbf{U}^*\mathbf{P}^* \tag{25}$$

and equation (25) is rewritten as

$$\tilde{\mathbf{G}}(\omega_m)\tilde{\mathbf{G}}^*(\omega_m) \approx \tilde{\mathbf{U}}\Sigma\Sigma^*\tilde{\mathbf{U}}^*. \tag{26}$$

Therefore, $\tilde{\mathbf{U}}$ is the left singular decomposition matrix of $\tilde{\mathbf{G}}(\omega_m)$

$$\tilde{\mathbf{U}} \approx \mathbf{P}\mathbf{U}\mathbf{P}^*. \tag{27}$$

According to the FDD method, the first column of $\tilde{\mathbf{U}}$ is an estimation of the mth mode shape, designated $\tilde{\mathbf{U}}_1$, and it can be expressed in terms of $\mathbf{U}_1$ as

$$\tilde{\mathbf{U}}_1 = \begin{bmatrix} e^{i\omega_m\delta t_1 - i\omega_m\delta t_1}\mathbf{U}_{1,1} \\ \vdots \\ e^{i\omega_m\delta t_i - i\omega_m\delta t_1}\mathbf{U}_{i,1} \\ \vdots \\ e^{i\omega_m\delta t_n - i\omega_m\delta t_1}\mathbf{U}_{n,1} \end{bmatrix}. \tag{28}$$

To normalize this mode shape $\tilde{\mathbf{U}}_1$, each component is divided by the reference component (say, the rth component) as

$$\tilde{\mathbf{U}}_1 \approx \begin{bmatrix} \frac{e^{i\omega_m\delta t_1 - i\omega_m\delta t_1}\mathbf{U}_{1,1}}{e^{i\omega_m\delta t_r - i\omega_m\delta t_1}\mathbf{U}_{r,1}} \\ \vdots \\ \frac{e^{i\omega_m\delta t_i - i\omega_m\delta t_1}\mathbf{U}_{i,1}}{e^{i\omega_m\delta t_r - i\omega_m\delta t_1}\mathbf{U}_{r,1}} \\ \vdots \\ \frac{e^{i\omega_m\delta t_n - i\omega_m\delta t_1}\mathbf{U}_{n,1}}{e^{i\omega_m\delta t_r - i\omega_m\delta t_1}\mathbf{U}_{r,1}} \end{bmatrix} = \begin{bmatrix} e^{i\omega_m(\delta t_1 - \delta t_r)}\frac{\mathbf{U}_{1,1}}{\mathbf{U}_{r,1}} \\ \vdots \\ e^{i\omega_m(\delta t_i - \delta t_r)}\frac{\mathbf{U}_{i,1}}{\mathbf{U}_{r,1}} \\ \vdots \\ e^{i\omega_m(\delta t_n - \delta t_r)}\frac{\mathbf{U}_{n,1}}{\mathbf{U}_{r,1}} \end{bmatrix} \tag{29}$$

where $\tilde{\mathbf{U}}_1$ denotes the mth mode shape identified from the response with TSEs, and $\mathbf{U}_{i,1}$ denotes the ith mode shape component that would be identified using synchronized data. δt_r is the TSE of the reference (or rth component).

From equation (29), it is clear that the presence of TSEs introduce a phase shift to each of the mode shape components, which is reflected in the term $e^{i\omega_m(\delta t_i - \delta t_r)}$ for the ith component. In addition, the TSEs introduce errors in the amplitude and the phase of each mode shape component, which is reflected in the use of '$\approx$'.

Note that this analysis evaluates the errors in the identified mode shapes when the FDD method is applied. The errors due to TSEs may have a different impact on the identified mode shapes when using other modal identification techniques. However, when the FDD method is used, the main source of error in the identified mode shapes is the phase shift present in each component in equation (29). In practice, other sources of error are negligible when typical TSEs are considered.

From equation (29), the non-negligible phase shift in the ith component is equal to $\omega_m(\delta t_i - \delta t_r)$. Note that the value of this error is based both on the TSEs and on the value of natural frequency ω_m. Therefore, higher order modes will exhibit larger phase shifts and larger distortions.

Based on this analysis, it is possible to estimate the acceptable TSE to avoid distortion in a given structural mode. If the phase shifts are small enough to keep the phase of the components of the normalized $\tilde{\mathbf{U}}_1$ in the same region ($[-\frac{\pi}{2} \quad \frac{\pi}{2}]$ or $[\frac{\pi}{2} \quad \frac{3\pi}{2}]$) as the normalized $\mathbf{U}_1$, the signs of mode shape components will not be changed. However, if the phase shift of one component in the normalized $\tilde{\mathbf{U}}_1$ is large enough to force the phase of this component into another range, for instance, from $[-\frac{\pi}{2} \quad \frac{\pi}{2}]$ to $[\frac{\pi}{2} \quad \frac{3\pi}{2}]$, the sign of this mode shape component will be different from the true one, and the identified mode shape will be distorted.

Because it is difficult to estimate TSEs between wireless sensors, especially for complex WSN configurations, one cannot easily obtain information on the phase shifts of mode shape components and thus cannot directly correct the distorted mode shapes. Alternatively, if one neglects phase information and assumes all the mode shape components have the same sign, the modified mode shapes can be used for damage detection. These modified mode shapes are the absolute values of the distorted mode shapes, referred to herein as absolute mode shapes (AMS). The distortion of identified mode shapes caused by TSEs and the capability of this strategy are illustrated in figure 2 using an example of a simply supported beam. This strategy is simple, but very useful when paired with an appropriate damage detection technique. It facilitates effective damage detection based on a WSN with large TSEs, and thus significantly prolongs the time synchronization period.
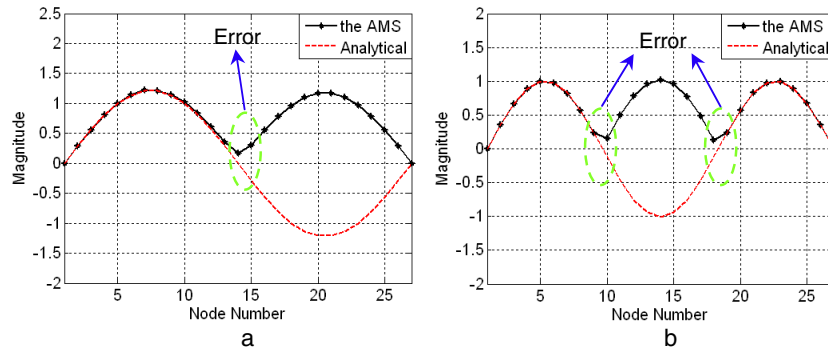
Figure 3. Comparison between AMSs and true mode shapes. (a) 2nd AMS after sign adjustment and (b) 3rd AMS after sign adjustment.

4. Problem formulation: damage detection strategies based on the distorted mode shapes and the AMSs

Following the above discussion of the impact of TSEs on the identified mode shapes, two approaches may be considered to accommodate these effects in the damage detection problem. One approach is to directly employ the distorted mode shapes, and the other is to apply the modified mode shapes (the AMS) for damage detection. The following approaches have been considered.

4.1. Damage detection using distorted mode shapes

Although the identified mode shapes may be distorted, recognizing that the signs of some mode shape components are changed, the classical flexibility difference method [20] is still applicable with distorted mode shapes. From equation (4), it is observed that each diagonal component in the flexibility matrix is a sum of n squared terms. Thus, if the signs of these mode shape components are incorrect, the diagonal elements of the constructed flexibility matrix **F** from these mode shapes will still be equal to the true values. Therefore, the damage indicators extracted from the diagonal entries of the flexibility matrix are not affected by TSEs when the distorted mode shapes are used to assemble flexibility matrices.

4.2. Damage detection using absolute mode shapes (AMS)

Because the classical flexibility difference method can be used with the distorted mode shapes, it can also be used with the AMSs. However, the method itself cannot localize damage to exact members. To achieve this goal, the ASH flexibility-based method is employed. Here equation (5) is still used to construct the ASH flexibility. However, the ASH mode shape is constructed by AMSs as

$$\mathbf{R}_r = [\; \tfrac{1}{l_1}|\varphi_{1,r}| \quad \tfrac{1}{l_2}(|\varphi_{2,r}| - |\varphi_{1,r}|) \quad \cdots \quad \tfrac{1}{l_i}(|\varphi_{i,r}| - |\varphi_{i-1,r}|)$$
$$\cdots \quad \tfrac{1}{l_n}(|\varphi_{n,r}| - |\varphi_{n-1,r}|) \;]^{\mathbf{T}} \qquad (30)$$

where $|\varphi_{i,r}|$ is the AMS component. The damage indicators are extracted from the difference in the ASH flexibility matrices before and after damage in the same way as in the original ASH flexibility-based method. The feasibility of applying the AMSs to the ASH flexibility-based method [21] is analyzed.
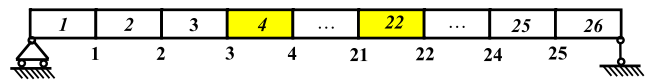

Figure 4. FEM of simply supported beam.

(1) Due to the sign adjustment in the AMSs, the magnitudes of the ASH mode shape components calculated from the AMSs are equal to those calculated from the real mode shapes, except for ASH mode shape components corresponding to elements near the nodes of modes, which will introduce some errors in the constructed ASH flexibility matrix. This effect is shown in figure 3 which displays the AMSs of a simply supported beam. For higher modes which have more nodes, the effect is greater. Fortunately, higher modes result in smaller contributions toward the ASH flexibility matrix.

(2) Although the signs of some components in ASH mode shapes calculated from the AMSs are not correct compared with the real ASH mode shapes, it is the same case for both the intact and damaged states.

Therefore, the ASH flexibility-based method is still effective when the AMSs are available. Because this method determines local ASH changes caused by damage, the damage indicators extracted from the difference in the ASH flexibility matrices constructed using the AMSs before and after damage are able to localize damage to exact elements.

5. Numerical simulations

5.1. Simply supported beam

To validate the performance of the proposed strategy, a simply supported beam is first studied numerically. This beam is assumed to be made of aluminum with dimensions 2080 mm × 20 mm × 20 mm. Young's modulus, the mass density and Poisson's ratio of the material are 70 Gpa, 2700 kg m^{-3} and 0.3, respectively. The beam is modeled using 26 beam elements, each of 80 mm long, with 27 nodes, as shown in figure 4. The first five analytical natural frequencies are shown in the first column of table 2.

Assume that energy dissipation is included as proportional viscous damping with a magnitude of 1% of critical in each
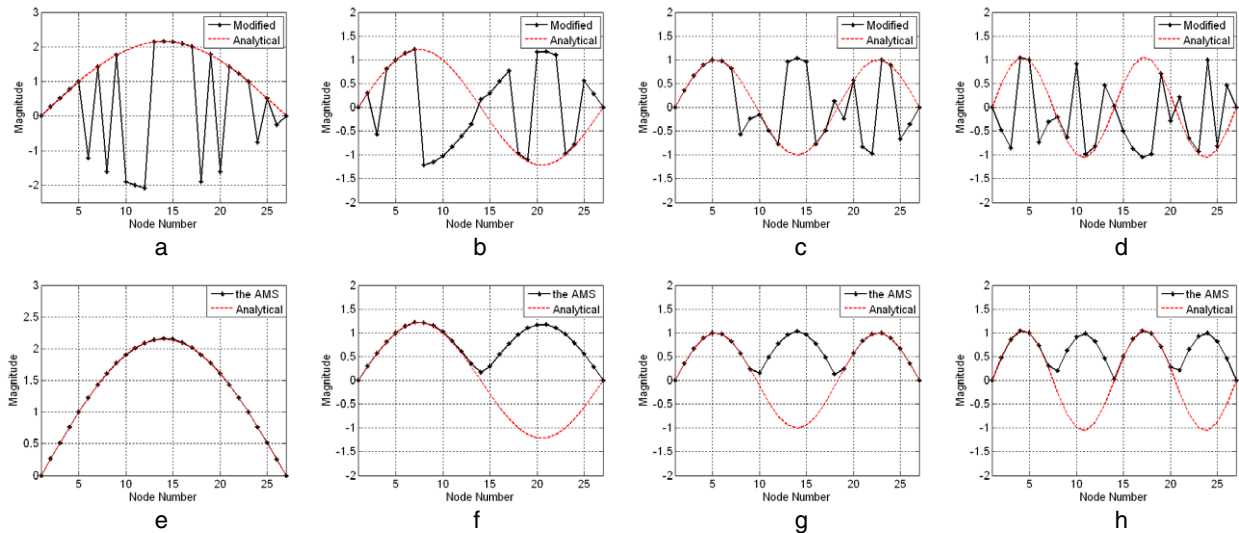
Figure 5. Influence of TSEs on identified mode shapes ((a)–(d)) and modified mode shapes ((e)–(h)). (a) 1st distorted mode, (b) 2nd distorted mode, (c) 3rd distorted mode, (d) 4th distorted mode, (e) 1st AMS, (f) 2nd AMS, (g) 3rd AMS and (h) 4th AMS.

Table 2. First five natural frequencies of simply supported beam (Hz). (Note: δt_{max} represents the maximum sampling delay between wireless sensors.)

			Identified results					
	Analytical		$\delta t_{max} = 10/1152$ s		$\delta t_{max} = 20/1152$ s		$\delta t_{max} = 50/1152$ s	
	Intact	Damaged	Intact	Damaged	Intact	Damaged	Intact	Damaged
1	10.67	10.49	10.69	10.41	10.69	10.41	10.69	10.41
2	42.59	40.54	42.47	40.50	42.47	40.50	42.47	40.50
3	95.54	89.40	95.06	89.44	95.06	89.44	95.06	89.44
4	169.13	160.12	169.88	159.75	169.88	159.75	169.88	159.75
5	262.84	255.36	262.13	254.53	262.13	254.53	262.13	254.53

mode of the structure. A band-limited white noise is applied vertically at all nodes to simulate ambient vibration. Simulated acceleration responses in the vertical direction are computed using Newmark-Beta integration. It is assumed that only the acceleration time history is recorded and the sampling rate is 1152 Hz. To simulate practical field conditions, Gaussian white noise with the mean value of zero and an RMS (root mean square) equal to 5% of the RMS of the responses is added to the acceleration responses.

5.1.1. Influence of time synchronization error on identified mode shapes. The intact structure is considered here. Errors in synchronization of the simulated wireless sensors are simulated by delaying acquisition of the response. A delay vector is generated randomly for the various sensor nodes, and the maximum value is set to 50/1152 s (50 time steps). The delay imposed on the acquisition of responses at each node is listed in table 3.

Using the FDD method, the first four mode shapes are identified using the simulated data with delays. These results are shown in figures 5(a)–(d). In each figure, the solid line represents the identified mode shape, and the dashed line represents the analytical mode shape. Obviously, the identified mode shapes are severely distorted. Several components

deviate significantly from the corresponding analytical modes. The amplitudes appear to be almost the same as the analytical modes, but several components have incorrect signs. This result is consistent with the discussion in section 3.

Using the strategy proposed in section 3, the associated AMSs are obtained and are presented in figures 5 (e)–(h). Note that these agree well with the absolute values of the analytical modes.

5.1.2. Damage localization. Damage is simulated as a 50% reduction of Young's moduli in elements 4 and 22. Three different cases are studied with random delays having maximum values of 10/1152 s, 20/1152 s and 50/1152 s, respectively. The first five natural frequencies identified in these three cases are shown in table 2. It is demonstrated empirically that TSEs in a WSN do not affect the identification results of natural frequencies, reinforcing the conclusions of prior researchers [14].

Both the ASH flexibility-based method and the classical flexibility difference method are employed here to localize damage in the simply supported beam. The procedure for localizing damage using the AMSs with the ASH flexibility-based method is as follows. The modal parameters are identified using the FDD method, and then the identified mode
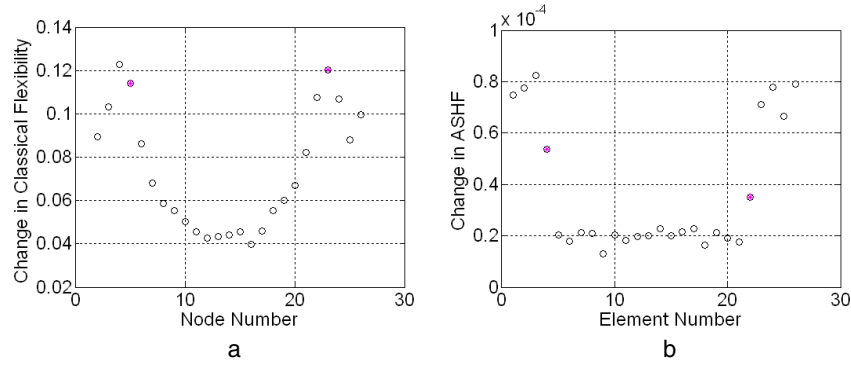
Figure 6. Damage localization results with maximum sampling delay of 10/1152 s. (a) Classical flexibility difference method and (b) ASH flexibility-based method.

Table 3. Simulated delays in data acquisition. (Note: '44' means acquisition of the data is delayed 44 time steps (i.e., $4/1152 = 0.0382$ s).)

	N1	N2	N3	N4	N5	N6	N7	N8	N9	N10	N11	N12	N13
Delay	44	29	42	21	17	44	0	27	9	8	6	36	48
	N14	N15	N16	N17	N18	N19	N20	N21	N22	N23	N24	N25	
Delay	50	30	29	16	49	5	36	27	20	10	35	2	
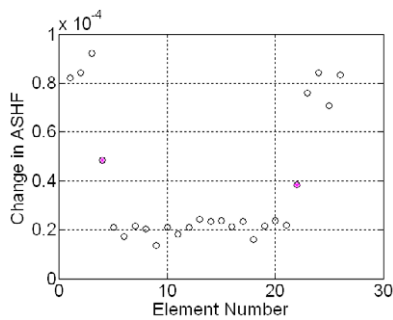
Figure 7. Damage localization results with maximum sampling delay of 20/1152 s.
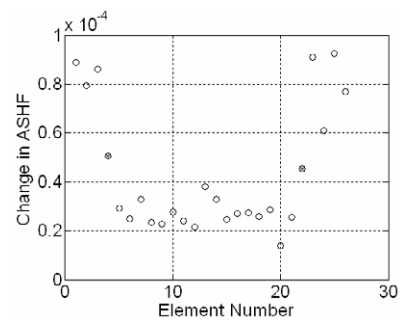
Figure 8. Damage localization results with maximum sampling delay of 50/1152 s.

shapes are used to obtain the AMSs. Next, the ASH flexibility matrix is constructed using the AMSs and natural frequencies, and the maximum absolute values of the components in each column of the difference between ASH flexibility matrices before and after damage are extracted as damage indicators. In each of the three cases, a different number of modes (three, four and five) are used to assemble the ASH flexibility matrix to explore the impact. Similar results are obtained with three, four or five modes, and thus representative results corresponding to using five modes are presented in figures 6–8. When the maximum sampling delays (designated $\delta t^{\max}$) are 10/1152 and 20/1152 s, the results demonstrate that the ASH flexibility-based method can easily localize the damage to the exact elements by observing 'step and jump' in a plot of damage indicators versus element number. When $\delta t^{\max}$ reaches 50/1152 s, the damage localization results are not as good as in the other two cases. This outcome occurs because, as $\delta t^{\max}$ increases, the errors in the magnitude of the identified mode shapes increase, which reduces the accuracy of the damage detection results. Based on the above observation,

the maximum sampling delay that the proposed strategy can tolerate is 50/1152 s (43.400 ms) for this structure, in terms of obtaining useful information to localize damage. If $\delta t^{\max}$ continues to increase, the errors will yield poor results.

The damage location results using the distorted mode shapes with the classical flexibility difference method for the first case are also presented in figure 6 for comparison. Although there are peaks around the two damage sites, it is difficult to precisely determine the damaged elements.

5.2. Planar truss

A 14-bay planar truss structure simply supported at the ends (see figure 9), is also considered to illustrate the ASH flexibility-based method using the AMSs. The cross-sectional area of each member is 1.122×10^{-4} m^2. Young's modulus, the mass density and Poisson's ratio of the material are 2×10^{11} Pa, 7850 kg m^{-3} and 0.3, respectively. The model has 28 nodes and 53 members. The numbering of elements and nodes of

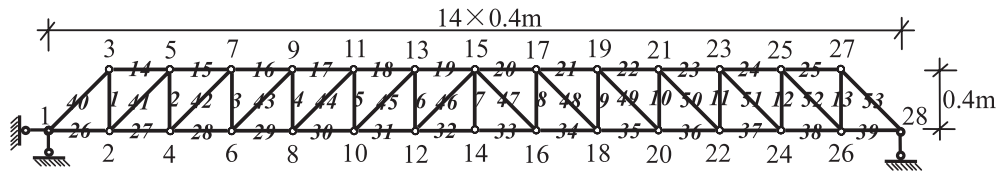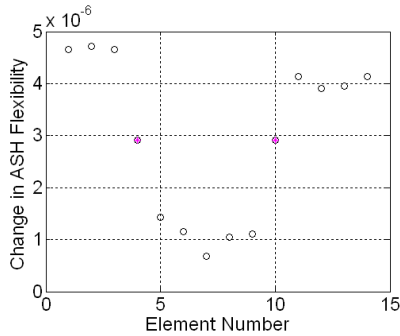**Figure 9.** 14-bay planar truss.

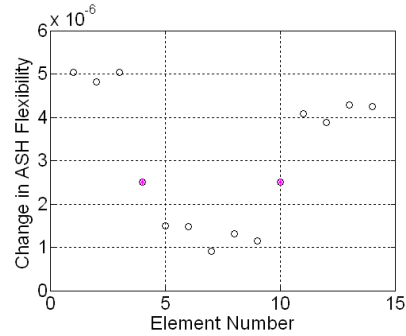**Figure 10.** Results using ASH flexibility when $\delta t^{\max}$ is 20/1152 s.
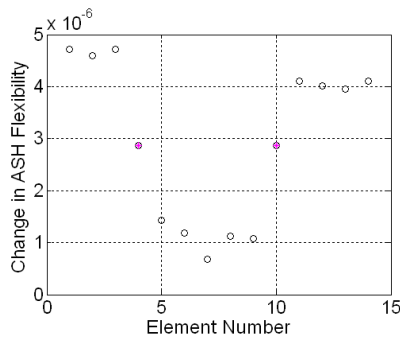

Figure 12. Results using ASH flexibility when $\delta t^{\max}$ is 200/1152 s.

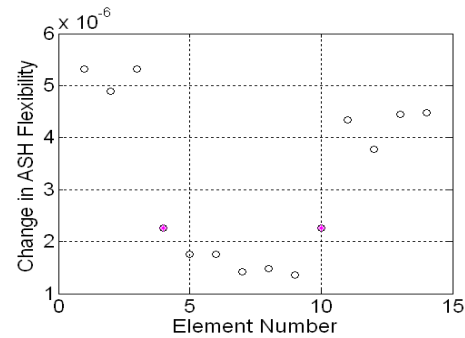**Figure 11.** Results using ASH flexibility when $\delta t^{\max}$ is 50/1152 s.

Figure 13. Results using ASH flexibility when $\delta t^{\max}$ is 300/1152 s.

the FEM is shown in figure 9. Lumped masses of 0.5 kg are applied on the 1st and 28th nodes, and 10 kg on all other nodes.

Simulation of a modal experiment is similar to that of the above numerical example. A band-limited white noise is applied in the horizontal and vertical directions at all nodes to excite the structure. The sampling frequency of acceleration response is 1152 Hz and the sampling duration is 60 s. The noise added to the response at each node is prescribed to have an RMS value equal to 5% of that of the corresponding response.

Damage is simulated as a 50% reduction in the cross-sectional area of the following members: members 16, 43 and 29 in the 4th bay, and members 22, 49 and 35 in the 10th bay. Several cases with different $\delta t^{\max}$ (20/1152, 50/1152, 200/1152 and 300/1152 s) are studied. The simulated acquisition delays representing TSEs are generated randomly as above. The identified frequencies do not change for the different cases. The first four identified natural frequencies are 8.72, 28.97, 42.75 and 57.66 Hz.

To use the ASH flexibility-based method, the truss is considered as a beam with 14 elements. Only the vertical

responses of the nodes at lower chords are used for identifying mode shapes. Different numbers of AMSs (one through four) are used to construct the ASH flexibility matrix. Similar results are obtained using a different number of AMSs. Thus, for each case, only representative damage localization results using the first four modes are presented, as shown in figures 10–13. When the maximum sampling delay is less than 200/1152 s, the damaged regions are identified accurately. As $\delta t^{\max}$ is increased to 300/1152 sec, the larger amplitude errors in identified mode shapes prohibit good damage localization results.
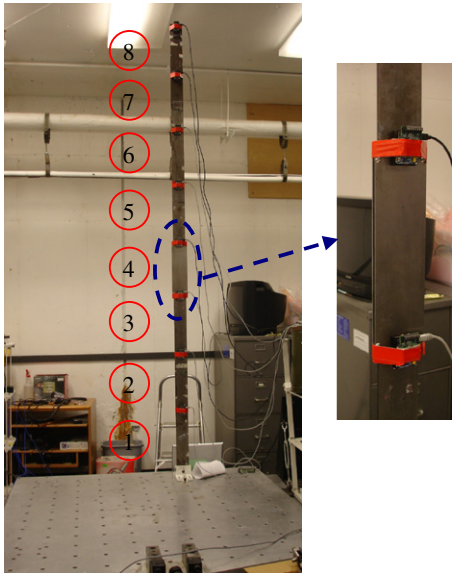
6. Experimental validation

To further demonstrate the effectiveness of the proposed strategy in practical applications, experimental tests are conducted on a steel cantilever beam at the Structural Control and Earthquake Engineering Laboratory at Washington University.

The beam is 108 inches long, 3 inches wide and 0.25 inches thick, as shown in figure 14. The numbers in the

Table 4. Actual sampling frequency of each sensor board.

	Node 1	Node 2	Node 3	Node 4	Node 5	Node 6	Node 7	Node 8
fs	280.72	280.23	286.43	298.44	293.61	277.30	300.45	294.69

Figure 14. Damaged cantilever beam and sensor placements in experiment.

Table 5. Identified natural frequencies of cantilever beam before and after damage.

Order	Intact (Hz)	Damaged (Hz)	Percentage change (%)
1	0.5864	0.5865	0.02
2	3.9580	4.1055	3.73
3	11.4341	11.4367	0.02

but also changes (increases) the stiffness of the structure, and accordingly, the flexibility. Modal experiments are performed on the intact and damaged beams, sequentially.

The acquired data from each sensor node is formatted in two columns. The first column represents the time stamps and the second column represents the acceleration response data. The actual sampling frequency of each wireless accelerometer node is calculated from the time stamps of each frame of data. From these tests, it is observed that the variation in sampling frequencies over time is very small, and the maximum deviation percentage is less than 0.04%. The average value of these sampling frequencies of all frames of data is taken as the sampling frequency of this sensor node. From the calculated sampling frequencies of all sensor nodes in one test, as shown in table 4, the sampling frequencies deviate from 280 Hz varying from sensor to sensor, and the maximum deviation percentage from 280 Hz is 7.30%. Therefore, a resampling operation has to be performed on the raw data before further processing the data. In this study, the maximum among the actual sampling frequencies is taken as the resampling frequency.

Because FTSP (FTSP is selected because it is a state-of-the-art protocol as well as the *de facto* standard time synchronization protocol in WSNs) has been embedded in the application, the resampled measured data can be taken as synchronized. First, the synchronized data is used for modal identification and damage localization. The FDD method is used to identify modal parameters. Table 5 presents the identified natural frequencies of the cantilever beam before and after damage. As we expect, the identified mode shapes are not distorted, as indicated by the black lines with squares in figure 16. The damage localization results using both the ASH flexibility-based method and the classical flexibility-based method are plotted in figure 15. From figure 15(a), the damage indicators are classified into two clusters, and the jump point between them suggests that element 4 is damaged, which is consistent with the actual damage scenario. When using the classical flexibility-based method with the distorted mode shapes, there is a peak around the damaged element, but it is difficult to determine the exact damaged element, as shown in figure 15(b).

To simulate the TSEs in the WSN, an acquisition delay is incorporated into each sensor's resampled data. Three
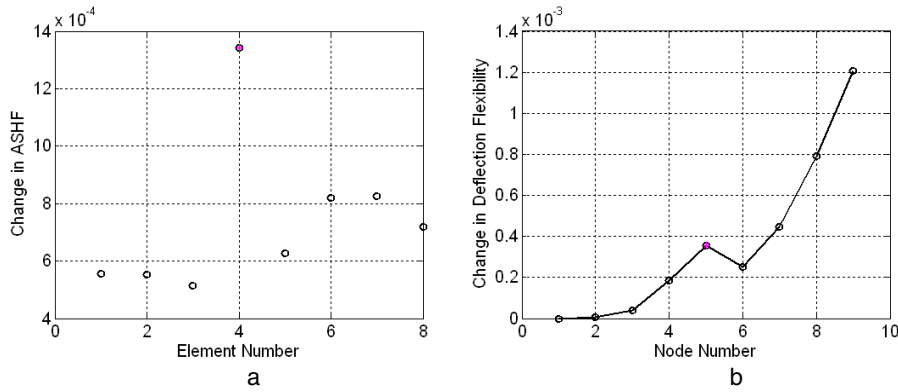
circles in this figure represent the element numbers. It is fixed to a shake table. Eight Intel Imote2 sensor platforms (IPR2400) with accelerometer boards and battery packs are used in these tests. Each Imote2 board is equipped with an integrated SRAM with 256 kB, an external SDRAM with 32 MB, an XScale CPU capable of running at the speed of up to 614 MHz, and an 802.15.4 radio (CC2420) as well as an antenna using 2.4 Hz[5]. Sensors are deployed uniformly along the beam to measure acceleration responses, as shown in figure 14. Before deploying the wireless sensors, the 'remotesensing' application developed by UIUC [24] is first uploaded to the Imote2 board of each sensor. For data collection, the sampling frequency of acceleration responses is set to 280 Hz, the number of sampling points is 12 288, and the size of each frame of data is 512. The wireless sensors transmit data packets to the PC base station through a gateway mote. The gateway mote consists of an Imote2 board and an interface board, and is connected to a PC with a USB cable. The sensors here are within a single hop of the base station.

The beam is excited along the weak axis of bending using an impact. The acceleration response data in this direction is collected at each node, and is transmitted to the PC. Then the PC performs modal identification and damage detection using MATLAB. Damage in the beam is simulated by adding a pair of thin, symmetric steel plates in element 4. They are 13.5 inch long, 3.625 inch wide and 0.0625 inch thick. Here the length of the added plates is equal to that of one element. In fact, adding mass here not only changes the mass of the structure,

[5] ITS400 Imote2 Basic Sensor Board, Crossbow Technology, Inc.

Figure 15. Damage localization results for cantilever beam using two flexibilities when the data is synchronized. (a) Maximum values in difference matrix of ASH flexibility and (b) diagonal elements of difference matrix of deflection flexibility.
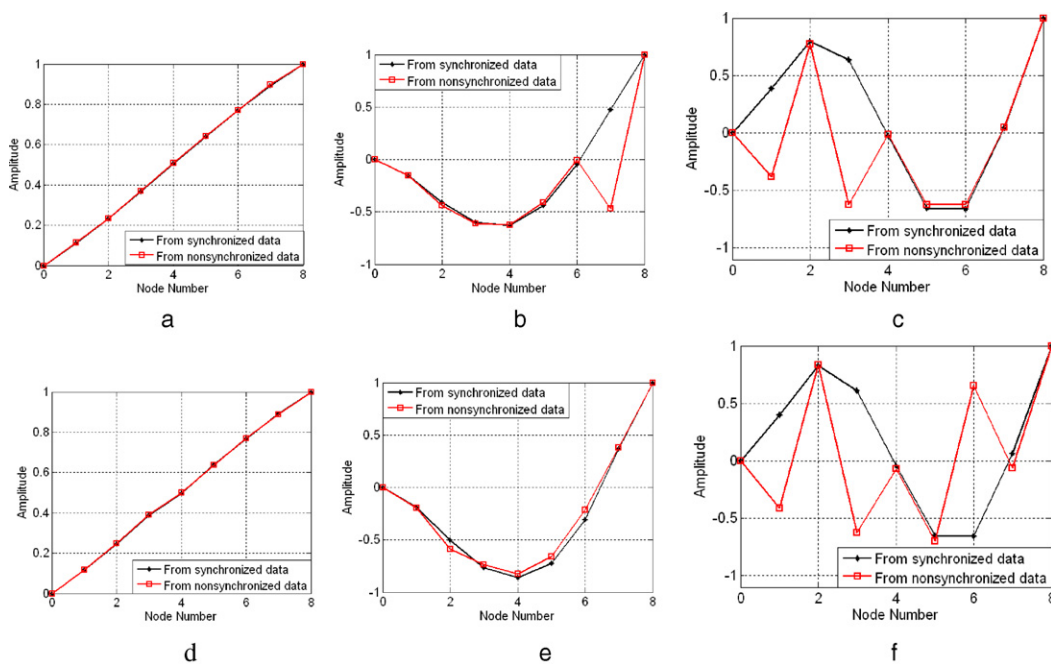

Figure 16. Identified modal parameters when δt^{max} is 20/280 s. (a) 1st mode of intact beam, (b) 2nd mode of intact beam, (c) 3rd mode of intact beam, (d) 1st mode of damaged beam, (e) 2nd mode of damaged beam and (f) 3rd mode of damaged beam.

cases with different δt^{max} (20/280, 30/280 and 40/280 s) are considered here, and different random delays are considered for the intact and damaged cases. For each case, both methods are used to localize damage.

The identified mode shapes for the case with a δt^{max} of 20/280 s are plotted in figure 16. In general, they are severely distorted. However, although the signs of some mode shape components are incorrect, their amplitudes are approximately correct, which verifies the discussion in section 3. To detect damage, the proposed strategy is first used to obtain the AMSs, and then the ASH flexibility matrix is constructed using the AMSs. Next, the damage indicators based on the ASH flexibility constructed by the first three modes are extracted. These values are presented in figure 17(a). The damage indicator of the fourth element exhibits a jump between two clusters of damage indicators, and thus clearly the damage of element 4 is identified.

The identified modal parameters and the damage localization results are presented in figures 18 and 19, respectively, for the case in which the δt^{max} is 30/280 s. Comparing figures 16 with figure 18, it is found that the distortion of the identified mode shapes in the latter is more severe, as the time synchronization errors increase. The damaged element can be identified using the ASH flexibility-based method with the first three modes, as shown in figure 19(a).

When δt^{max} reaches 40/280 s, the identified mode shapes are severely distorted. The damage localization results when the first mode is used are shown in figure 20. Obviously, the accuracy of damage localization is reduced due to the relatively large error in amplitude caused by the TSEs.

Based on the observations discussed above, two main conclusions can be drawn. First, the proposed strategy is tolerant of time synchronization errors of up to 30/280 s
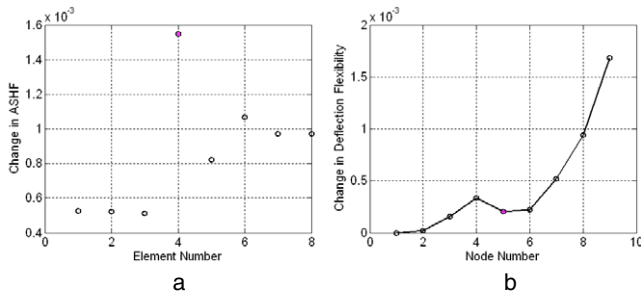
Figure 17. Damage localization results for cantilever beam using two flexibilities when δt^{max} is 20/280 s. (a) Maximum values in the difference matrix of ASH flexibility and (b) diagonal elements of the difference matrix of deflection flexibility.

Figure 19. Damage localization results for cantilever beam using two flexibilities when δt^{max} is 30/280 s. (a) Maximum values in the difference matrix of ASH flexibility and (b) diagonal elements of the difference matrix of deflection flexibility.

for this beam. However, using traditional damage detection methods, a TSE of less than 4/280 s hinders correct modal identification and damage detection results. Thus, the proposed strategy facilitates prolonging the time re-synchronization period significantly. The second conclusion is that the ability to perform damage localization with the ASH flexibility-based method using AMSs is more effective than the classical flexibility-based method with distorted mode shapes.

7. Conclusions

Time synchronization errors (TSEs) attributed to clock drifts and clock offsets in a WSN have an impact on both the amplitudes and phases of the identified mode shapes. The largest error in the mode shapes, and the one that must be considered in practice, is the significant phase shif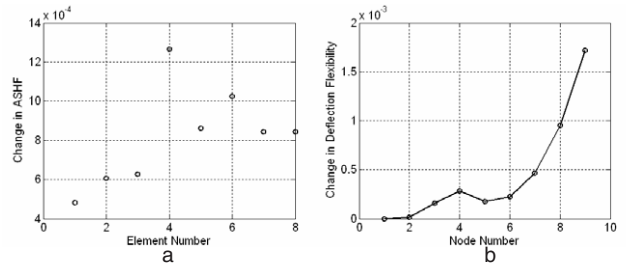t at each sensor node. TSEs can be minimized by frequently implementing time synchronization protocols. However, this requires a significant amount of energy. Here we alleviate this technical challenge from a new perspective. A damage localization strategy that is tolerant of TSEs is proposed to reduce the time synchronization frequency. First, the distortion in the identified mode shapes caused by the TSEs is investigated, and then a strategy is developed for modifying the distorted mode shapes for use in damage detection. Then the modified mode shapes are utilized with the ASH flexibility-based damage detection method to perform damage localization at the member level. Numerical simulation results of a simply supported beam and a planar truss demonstrate that the aforementioned proposed strategy is able to tolerate significant time synchronization errors, and thus can relax the requirement of frequent sensor synchronization in WSNs without sacrificing accuracy in modal identification and damage localization results. The use of the proposed approach that allows for prolonging the time re-synchronization period has been validated through experimental tests in the laboratory.
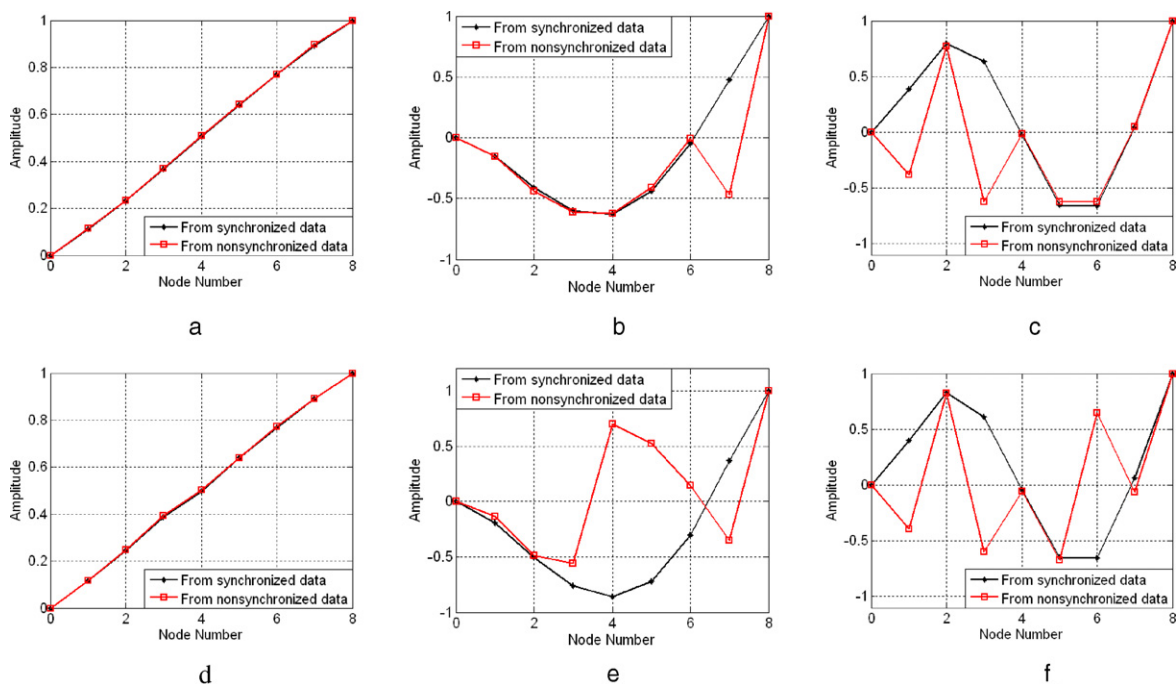

Figure 18. Identified modal parameters when δt^{max} is 30/280 s. (a) 1st mode of intact beam, (b) 2nd mode of intact beam, (c) 3rd mode of intact beam, (d) 1st mode of damaged beam, (e) 2nd mode of damaged beam and (f) 3rd mode of damaged beam.
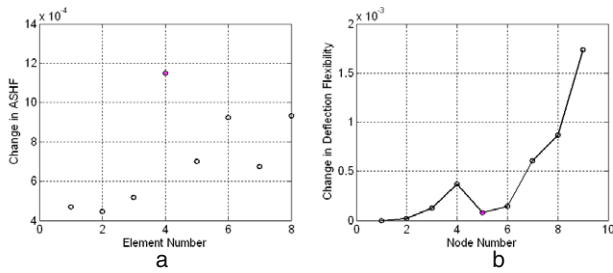
Figure 20. Damage localization results for cantilever beam using two flexibilities when $\delta t^{\max}$ is 40/280 s. (a) Maximum values in the difference matrix of ASH flexibility and (b) diagonal elements of the difference matrix of deflection flexibility.

Acknowledgments

References

[1] Horton M A, Glaser S and Sitar N 2002 Wireless networks for structural health monitoring and hazard mitigation *Proc. US-Europe Workshop on Sensors and Smart Structures Technology* pp 19–23

[2] Lynch J P, Kiremidjian A S, Law K H, Kenny T and Carryer E 2002 Issues in wireless structural damage monitoring technologies *Proc. 3rd World Conf. on Structural Control* vol 2, pp 667–72

[3] Spencer B F 2003 Opportunities and challenges for smart sensing technology *1st Int. Conf. on Structural Health Monitoring and Intelligent Infrastructure (Tokyo, Nov. 2003)*

[4] Castaneda N, Dyke S, Lu C, Sun F and Hackmann G 2008 Experimental deployment and validation of a distributed SHM system using wireless sensor networks *Struct. Eng. Mech.* **32** 6 (August 20 2009)

[5] Hackmann G, Sun F, Castaneda N, Lu C Y and Dyke S 2008 A holistic approach to decentralized structural damage localization using wireless sensor networks *The 29th IEEE Real-Time Systems Symp. (Barcelona, Nov. 2008)*

[6] Weng J-H *et al* 2008 Output-only modal identification of a cable-stayed bridge using wireless monitoring systems *Eng. Struct.* **30** 1820–30

[7] Nagayama T, Sim S-H, Miyamori Y and Spencer B F Jr 2007 Issues in structural health monitoring employing smart sensors *Smart Struct. Syst.* **3** 299–320

[8] Shamim N P, Gregory L F, Sukun K and David E C 2008 Design and implementation of scalable wireless sensor network for structural monitoring *ASCE J. Infrastruct. Eng.* **14** 89–101

[9] Farrar C, Allen D, Park G, Ball S and Masquelier M 2006 Coupling sensing hardware with data interrogation software for structural health monitoring *Shock Vib.* **13** 519–30

[10] Elson J, Cirod L and Estrin D 2002 Fine-grained network time synchronization using reference broadcasts *Proc. 5th Symp. on Operating Systems Design and Implementation (Boston, MA)*

[11] Ganeriwal S, Kumar R and Srivastava M B 2003 Timing-sync protocol for sensor networks *SenSys; The 1st ACM Conf. on Embedded Networked Sensor System (Nov. 2003)* pp 138–49

[12] Maroti M, Kusy B, Simon G and Ledeczi A 2004 The flooding time synchronization protocol *SenSys: Proc. 2nd CAN Conf. on Embedded Networked Sensor Systems (Baltimore, MD, 2004)* pp 39–49

[13] Ping S 2003 *Delay Measurement Time Synchronization for Wireless Sensor Networks* Intel Research Berkeley lab, IRB-TR-03-013, June 2003

[14] Nagayama T 2007 Structural health monitoring using smart sensors *PhD Dissertation* University of Illinois at Urbana-Champaign

[15] Krishnamurthy V, Fowler K and Sazonov E 2008 The effect of time synchronization of wireless sensors on the modal analysis of structures *Smart Mater. Struct.* **17** 1–3

[16] Brinker R, Zhang L M and Andersen P 2000 Modal identification from ambient responses using frequency domain decomposition *IMAC: Proc. 18th Int. Modal Analysis Conf. (San Antonio, TX, 2000)* pp 625–30

[17] Pandey A K and Biswas M 1994 Damage detection in structures using change in flexibility *J. Sound Vib.* **169** 3–17

[18] Bernal D and Gunes B 2004 Flexibility based approach for damage characterization: benchmark application *J. Eng. Mech.* **130** 61–70

[19] Gao Y and Spencer B F 2002 Flexibility-based damage location employing ambient vibration *Proc. 15th ASCE Engineering Mechanics Conf. (New York)*

[20] Pandey A K and Biswas M 1995 Experimental verification of flexibility difference method for locating damage in structures *J. Sound Vib.* **184** 311–28

[21] Yan G, Duan Z and Ou J, Structural damage detection using the angle-between-string-and-horizon flexibility *Struct. Eng. Mech.* submitted

[22] Shamm N P, Gregory L F, Sukun K and David E C 2008 Design and implementation of scalable wireless sensor network for structural monitoring *J. Infrastruct. Syst.* **14** 89–101

[23] Kerschen G and Golinval J C 2002 Physical interpretation of the proper orthogonal modes using the singular value decomposition *J. Sound Vib.* **249** 849–65

[24] ISHMP 2008 Illinois Structural Health Monitoring Project. See software distribution at http://shm.cs.uiuc.edu/software.html